A structure-based algorithm for automated separation of subchondral bone in micro-computed tomography data

Ida Ang[a], Maria Fox[b], John D. Polk[b,c], and Mariana E. Kersh[d,e]

[a]Department of Bioengineering; [b]Department of Anthropology; [c]Department of Surgery; [d]Department of Mechanical Science and Engineering; [e]Beckman Institute for Advanced Science and Technology; University of Illinois at Urbana-Champaign, Urbana, Illinois, 61801, USA

ARTICLE HISTORY
Compiled August 25, 2018

ABSTRACT
Structural measurements of subchondral and trabecular bone are of interest for a wide variety of communities ranging from anthropology to biomechanical engineering, yet continues to be a challenge partly because of the lack of automated techniques for use with high resolution data. Here we present a structure-based algorithm for separating cortical compartments from trabecular bone in binarized images. Using the thickness of the cortex as a seed value, bone connected to the cortex within a spatially local threshold value is identified and separated from the remaining bone. The algorithm was tested on biological images from human, chimpanzee, and gorilla datasets and compared to manual measurements. The average error was 2-3 voxel differences in thickness and total area errors were less than ten percent. The algorithm is repeatable, efficient, and requires few user inputs, providing a means of separating cortical from trabecular bone. The Matlab code, example images, and datasets can be downloaded from uitbl.mechse.illinois.edu.

KEYWORDS
Bone; Image processing; Segmentation; Subchondral; Cortical

1. Introduction

Micro-computed tomography (micro-CT) is a primary source of structure and composition information of mineralized tissues for analyses of bone properties (Currey 2002). The increase in micro-CT availability and capacity, coupled with increased computational resources in research and clinical settings, has allowed for both cross-sectional and longitudinal studies to evaluate spatially local changes in bone under a variety of conditions. The (re)modeling response of bone to mechanical loading has been a longstanding subject of interest and has applications spanning from anthropology to medicine (Huiskes et al. 2000; Carlson et al. 2013; Wolff 1892; Currey 2002; Kivell 2016; Polk et al. 2008b; Su 2011; Müller-Gerbl et al. 1992; Polk et al. 2008a).

While the analysis of diaphyseal cortical properties are relatively straightforward, analyses of the epiphyses of bone remain challenging because of the simultaneous hierarchal and heterogeneous structure of bone. A rigorous assessment of cortical, subchondral, and trabecular properties requires separating these regions for independent

CONTACT M. E. Kersh Email: mkersh@illinois.edu

analyses. However, quantifying cortical bone thickness is difficult in regions where the trabecular mesh is highly complex and closely connected to the outer shell of bone. This is especially problematic in the epiphyses of bone, where subchondral bone, the thin layer of cortical bone underlying the joint articular cartilage (Radin et al. 1970; Pugh et al. 1974), is much thinner than bone at the diaphysis.

To avoid misidentifying subchondral bone as trabecular bone, volumes of interest (VOIs) at the center of the joint geometry have been used (Ryan and Ketcham 2002; Fajardo et al. 2007; Ryan and Walker 2010; Su et al. 2013). However, bone functional signals may be lost within this central region, and the clearest signal is likely to be present close to the joint surface (Fox et al. 2016; Polk et al. 2008b). Accounting for the spatial variation in micro-structure throughout the entire bone, in contrast to single isolated VOI-based analyses, may be a critical determinant for understanding how bone adapts to changes in mechanical loading.

While there have been significant advances in the imaging capacity of micro-CT, the methods needed to analyze the resulting data require further development. Several algorithms of varying complexity have been proposed to separate the cortex from the remaining trabecular structure. These algorithms rely on a combination of threshold-based techniques combined with morphological closing and opening operations to generate an external and internal shell. With all micro-CT imaging, variation will exist between scans, laboratories, and specimens, and the threshold values likely need to be tuned for different datasets. The analysis from Buie et al. shows that a small set of dual-threshold values could be used to reliably segment cortical bone in a variety of samples at different resolutions (Buie et al. 2007). However, variation due to scanner drift will require that the threshold values be periodically tuned for optimal results. There is the inevitable need to segment bone as an initial step for the aforementioned algorithms including the one we propose here. The use of different segmentation schemes based on global, local, or adaptive threshold values has been widely discussed in the literature and the reader is referred to (Pal and Pal 1993) for a review of these methods.

Once an optimal segmentation is achieved, we propose that the resulting binarized structural information can be used to separate the cortical compartment from the remaining bone. Here we present a simple automated approach using the BoneJ plug-in available with ImageJ (Doube et al. 2010) and MATLAB (MathWorks, Natick, MA) to first identify an image border of bone and then find bony components connected to the outer shell alone.

2. Methods

2.1. *Image input requirements*

Two input datasets are required: (1) a binary image (Fig. 1A) and (2) a thickness map (matrix) of the structures within the image (Fig. 1C). Thickness maps were obtained from the binarized image stacks using the ImageJ plugin, BoneJ (Hildebrand and Rüegsegger 1997; Doube et al. 2010). The resulting thickness image was saved as a text file and imported into MATLAB. Voxels with no data (NaN) were assigned zero.

2.2. *Image border detection*

Similar to Buie (Buie et al. 2007), we assume that an external cortical shell of bone exists as a continuous surface. However, it is not uncommon to have regions of cortical

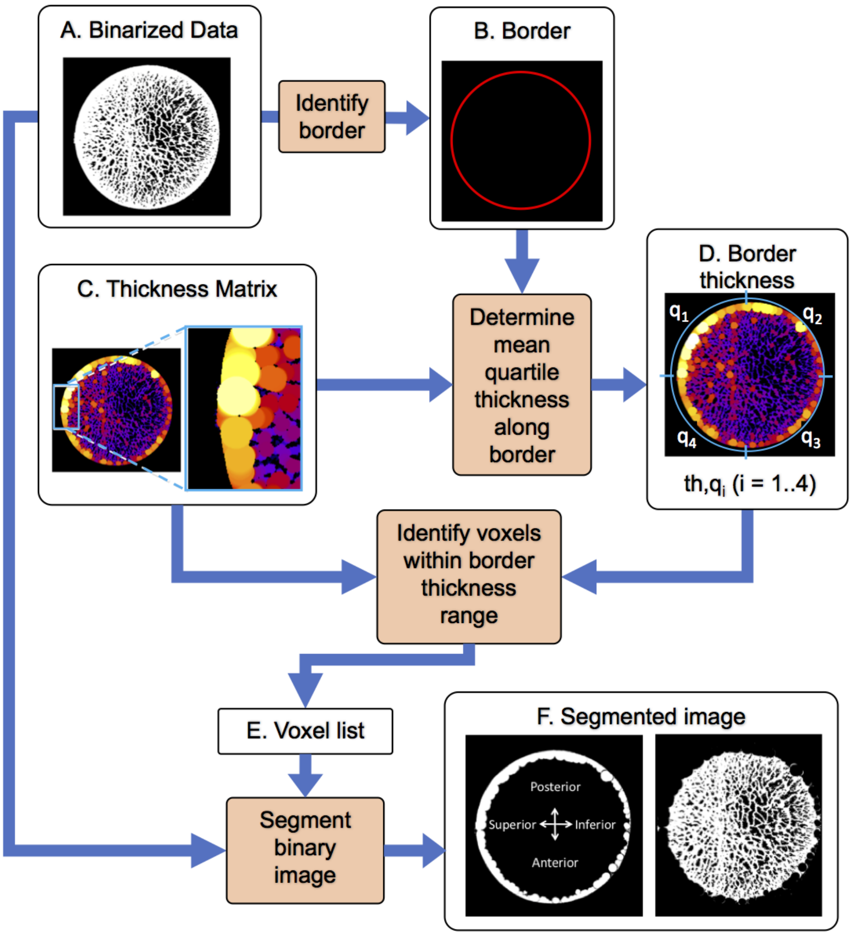

Figure 1.: General workflow of algorithm based on two user inputs, binarized data and thickness matrix obtained from ImageJ plugin, BoneJ. Example images from the human femoral head.

bone that are as thin as the surrounding trabecular bone, or are undetectable in the initial segmentation due to image noise or partial volume effects. Similarly, gaps in cortical bone may exist in pathological specimens (e.g., osteoporotic bone) or specimens from museum collections. These image artifacts may result in errors in the detection of a continuous border.

Therefore, we implemented an initial border check to ensure that a continuous border exists within the image by estimating a maximum border length and comparing it to the border within the image. The maximum border length was calculated using the extrema points of the binarized image to calculate the maximum distance from top to bottom, X_{est}, and from right to left, Y_{est}, as seen in Figure 2. The extrema points are connected to form triangles enclosing rough quadrants of the object border. This evaluation of the border is based on the assumption that the external contour of bone is convex or concave, not undulating; and therefore, the summation of the opposite and adjacent sides of the triangle will always be larger than the border. These maximum distances were used to calculate a maximum perimeter, B_e, using Eq. 1.

$$B_e = 2(X_{est} + Y_{est}) \tag{1}$$

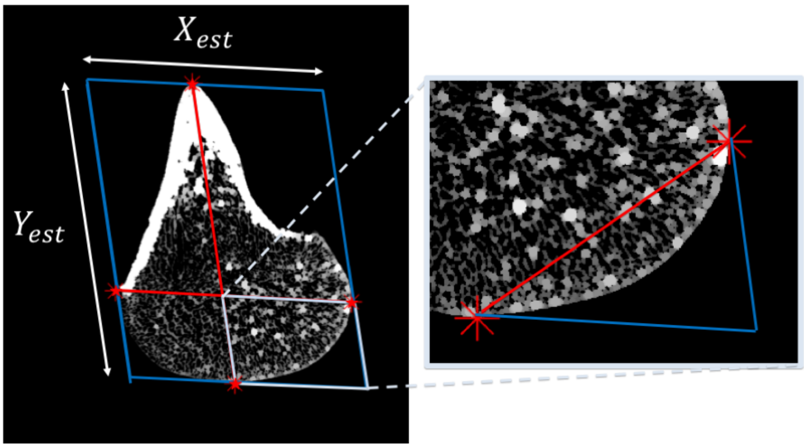

Figure 2.: Rectangular estimation of the border, B_e, calculated from extrema points for the lateral condyle of a chimpanzee.

The maximum rectangular perimeter value, B_e, was then compared to the initial calculation of the external border using MATLAB (function *bwboundaries*, version R2017A, Mathworks, Natick, MA, USA). If the border length is larger than the rectangular estimate, a warning is issued that the border should be corrected to fill gaps or holes that typically cause an overestimation of the border. These can be corrected using morphological erosion and dilation operations or other corrective options available within image processing software packages.

2.3. *Thickness-based separation*

The thickness matrix, based on measurements of the thickness of all objects within an image, was used to extract regions connected to the outer border that are of similar local thickness values. For any given pixel, p, along the boundary, the thickness (th_p) of bone was identified from the thickness matrix (Figure 1C).

The bone border was then sectioned into quadrants (Figure 1D), and the average of all non-zero thickness values at each quadrant was calculated, th_q. The average quadrant thickness, th_q, containing the pixel of interest was then used to determine the range of thickness values to include in the segmentation (Eq. 2). Next, a subset of pixels, p_s, to evaluate was identified by centering a window equal to 10% of the image width and length around the pixel of interest. Within this window, half of the global minimum thickness th_{min} value of each quadrants average thickness value was used as an upper and lower threshold to identify pixels of similar local thickness to the pixel of interest according to Eq. 2:.

$$p_{ss} = (th_p - \frac{th_{min}}{2} \times th_q) < p_s < (th_p + \frac{th_{min}}{2} \times th_q) \tag{2}$$

where p_{ss} is the total subset of pixels, p_s, within the range associated with the pixel on the border, th_p, and th_{min} is the global minimum thickness value.

This process was then repeated for every th_p, continuing clockwise to the next location, *i+1*, along the entire boundary (Fig. 3). For each pixel evaluated, the connectivity of the results was verified to ensure that the pixel of interest was included in each subsequent calculation. The resulting subsets were then merged into the final segmented image (Fig. 3D) which was then smoothed by eroding and dilating the image using a disc structural element (Fig. 3E). The algorithm was tested using a computer with two Xeon E5-2667 V4 Broadwell model processors with a total of 32 threads available.

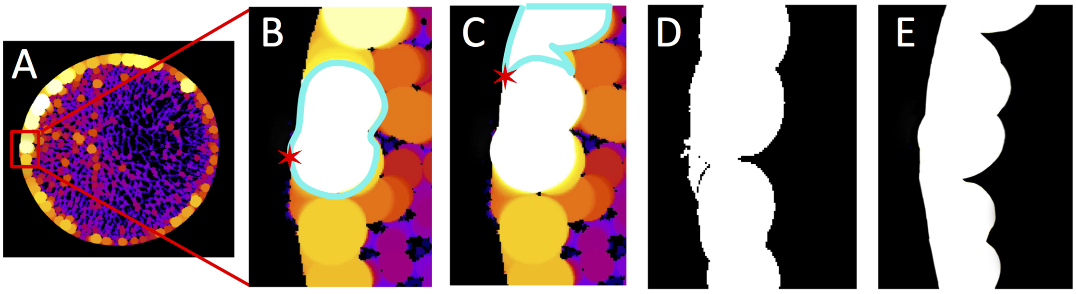

Figure 3.: Using the thickness matrix visualized in (A), the first pixel on the border (red asterisk in B) was identified and a subset of pixels within the set range (teal region) is shown on the thickness image. (C) Consecutive border pixel with corresponding areas. (D) The pixels identified were added to the previous cortical bone image to create a final segmented image (E).

2.4. *Evaluation: Biological images*

We evaluated the accuracy of the algorithm using high-resolution micro-computed tomography data sets: data from the human proximal femur was subdivided into the femoral head (n= 50 slices, Fig. 4A) and neck (n = 50 slices, Fig. 4B) and the chimpanzee lateral condyle (n = 41 slices, Fig. 4C). The human femur data was of isotropic voxel size, 0.049 mm, and the chimpanzee data had a pixel size of width, height = 0.05 mm and voxel depth of 1 mm. In the human femoral data, the data was aligned to the femoral neck axis after which portions of the femoral head and neck were analyzed separately. These species were selected to evaluate the utility of the algorithm across specimens with broad variation in cortical and trabecular thickness (Carlson and Patel 2006).

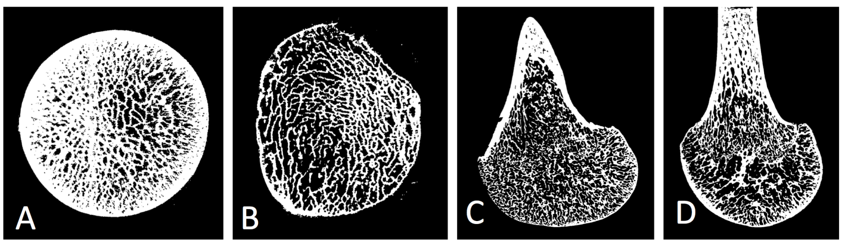

Figure 4.: Biological images for evaluation of algorithm accuracy. (A) Human femoral head, (B) femoral neck, (C) chimpanzee lateral condyle, and (D) gorilla lateral condyle

We also evaluated our algorithm on a dataset without a closed border, such as those slices found at a mid-slice through the bone, as an example of a worst-case scenario. To do so, we ran the algorithm on the mid-section of a lateral condyle from a set of gorilla CT data with in-plane voxels of 0.05 mm and depth of 1 mm (Fig. 4D).

The accuracy of the segmentation was quantified by comparing the results from our algorithm to a "gold standard" segmentation method of hand contouring using the segmentation editor plugin in Fiji. For manual segmentation, 11 images from each dataset was taken at regular intervals. All data was checked for normality using a Shapiro-Wilks test (alpha = 0.05). The mean absolute percent error in the area between measurements from our algorithm and manual contouring was calculated. We further subdivided images into quadrants and calculated the mean error in local thickness measurements. All statistical analyses were performed using R Studio (version 1.1.447, R-Studio, Inc).

3. Results

The algorithm was able to segment variably thick cortex as well as uniformly thick and thin cortices. Representative images from all data sets demonstrate the algorithm adjusting from thicker cortical bone to almost non-existent cortical bone within a given slice (Fig. 5). The femoral head data was relatively thick and uniform in many slices (Fig. 5A) while the femoral neck data reveals the thin cortices that are known to characterize this region of the proximal femur (Fig. 5B).

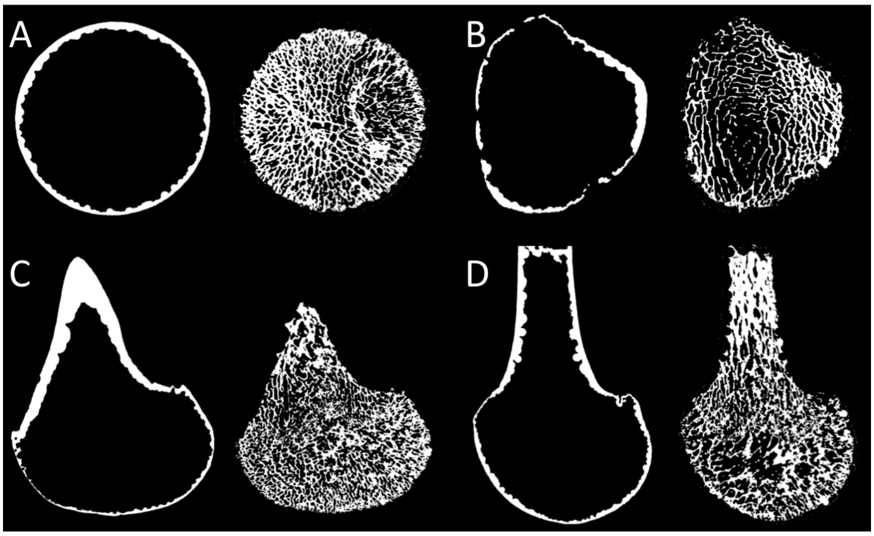

Figure 5.: Resulting cortical bone segmentation and the remaining trabecular bone are shown in sequence for (A) human femoral head, (B) femoral neck, (C) chimpanzee lateral condyle, and (D) gorilla lateral condyle CT sample images.

The median processing time for the algorithm was 46.5 ± 12.7 seconds, and was over ten times faster than the time required to manually segment the images (570 ± 128 seconds). The processing time for both manual and algorithm based segmentation was dependent on the complexity of the data (Table 1). The femoral head dataset, which was fairly uniform in thickness, took the least amount of time to segment. In contrast, the human femoral neck was more variable in thickness within a given slice, and took nearly twice as long to process. As a larger species, the gorilla data set also took longer to process than the femoral head and chimpanzee data.

Table 1.: Algorithm-based and manual segmentation time and mean absolute percent error in area measurements in the femoral head, neck, chimpanzee, and gorilla datasets.

Dataset	Average time per slice (sec)		Error in area (%)
	Algorithm	Manual	
Femoral head	27	420	5.64
Femoral neck	53	730	6.56
Chimpanzee	40	540	3.22
Gorilla	54	600	9.01

All data was found to be normally distributed. The mean absolute error in area measurements across all datasets was 5.81 $\pm$ 2.17% and the largest error was in the gorilla dataset (Table 1). The algorithm tended to overestimate the area of the femoral head and chimp condyle while the area in the femoral neck was underestimated by our algorithm. In general, the algorithm was successful in following increasing or decreasing areas along a given dataset (see Fig. 6B,C).

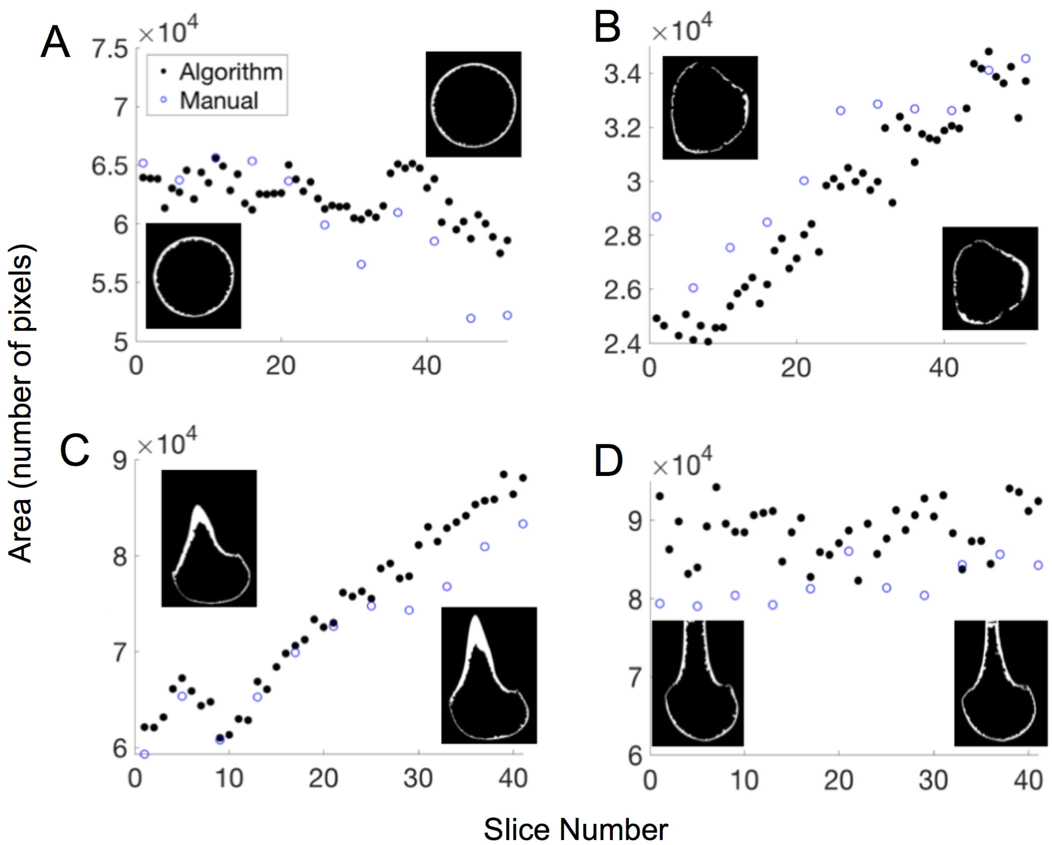

Figure 6.: Comparison between manual and algorithm cortical bone segmentation results for chimpanzee and femoral head and neck datasets. The percentage error between the manual and algorithm segmentation are displayed in a histogram (A) femoral head, (B) femoral neck, and (C) chimpanzee lateral condyle datasets.

With regards to thickness measurements, the average difference in femoral neck thickness calculations - compared to manual measurements - was less than one voxel (50 microns). Similar results were found for the gorilla dataset with the exception of the anterior aspect which had an average error of 100 microns. The femoral head dataset had similar error ranges (32-90 micron differences), and finally the chimpanzee had the highest differences in thickness with a maximum difference of 434 microns in the superior compartment.

Table 2.: Difference between manual and algorithm-based segmentation

Dataset	Mean Difference (µm)			
	Posterior	Inferior	Superior	Anterior
Head	-71 ± 114	90 ± 114	-54 ± 94	32 ± 141
Neck	2 ± 58	-37 ± 137	-20 ± 39	13 ± 58
Chimpanzee	-98 ± 46	-153 ± 63	434 ± 300	232 ± 192
Gorilla	-17 ± 28	-29 ± 50	14 ± 67	100 ± 83

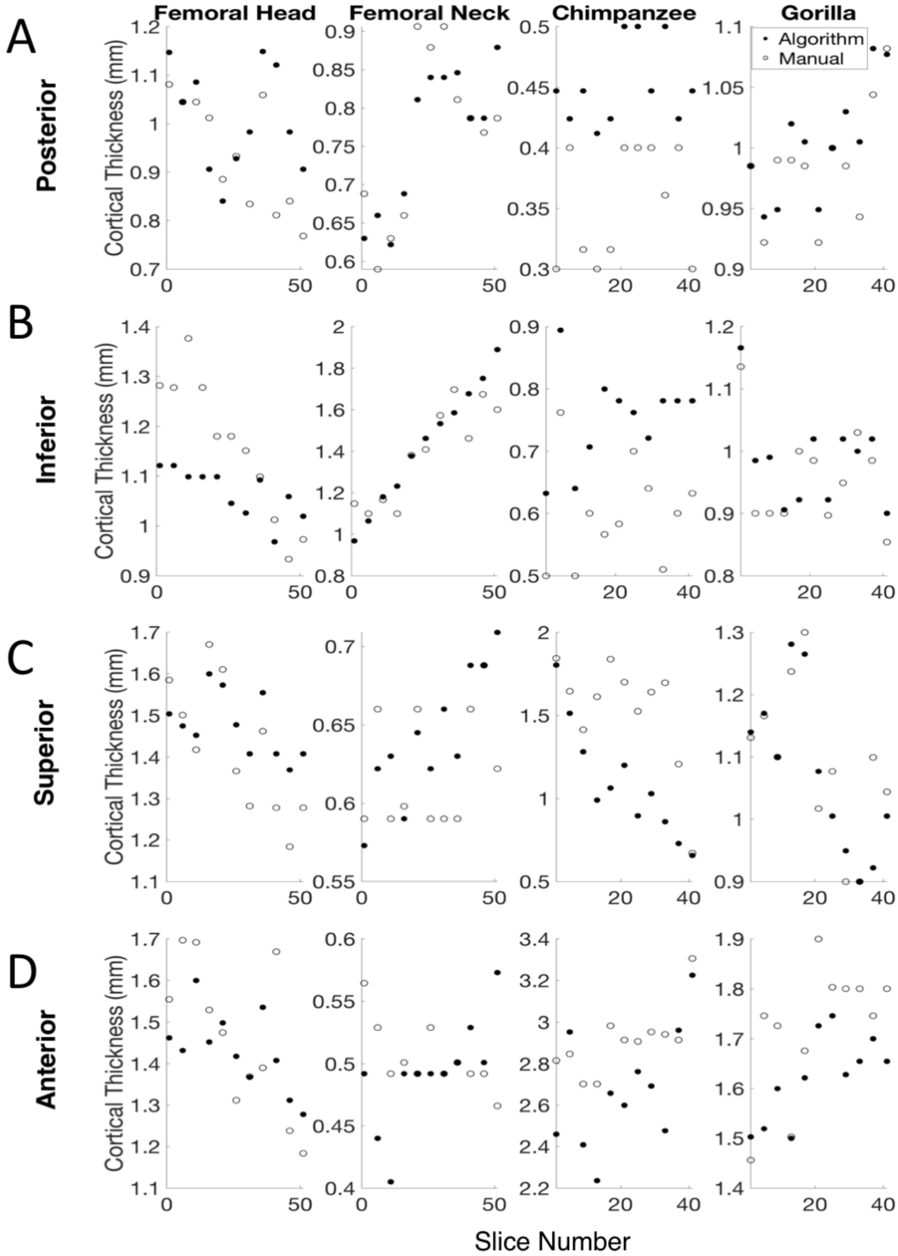

Figure 7.: Local cortical thickness measurements within the femoral head and neck, and chimpanzee and gorilla lateral condyle. Measurements are based on mean thickness within each quadrant.

4. Discussion

We have presented a structure-based methodology for segmenting cortical or subchondral bone from binarized micro-computed tomography images. The overestimation of the border in the femoral head, chimp condyle and remaining sections of the gorilla data was due to inclusion of cortical segments that extended into the trabecular region of bone (see magenta regions in Figure 8A,C, and D). The underestimation of the border in the femoral neck was the result of gaps in our binarized images that were not found during the manual segmentation of the grayscale images Figure 8B). The overestimation in the gorilla dataset was attributable to the inclusion of a section of trabecular bone towards the open border which our algorithm included as part of the cortical border (Figure 8D).

As expected, local thickness measurements were more variable between our algorithm and manually derived measurements. The algorithm performed quite well in datasets except for the chimpanzee condyle. Within the inferior and posterior regions, the algorithm tended to overpredict thickness values while the superior and anterior regions were underpredicted. Our visual inspection of the images did not reveal any trends to explain these differences, and the qualitative results remained acceptable.

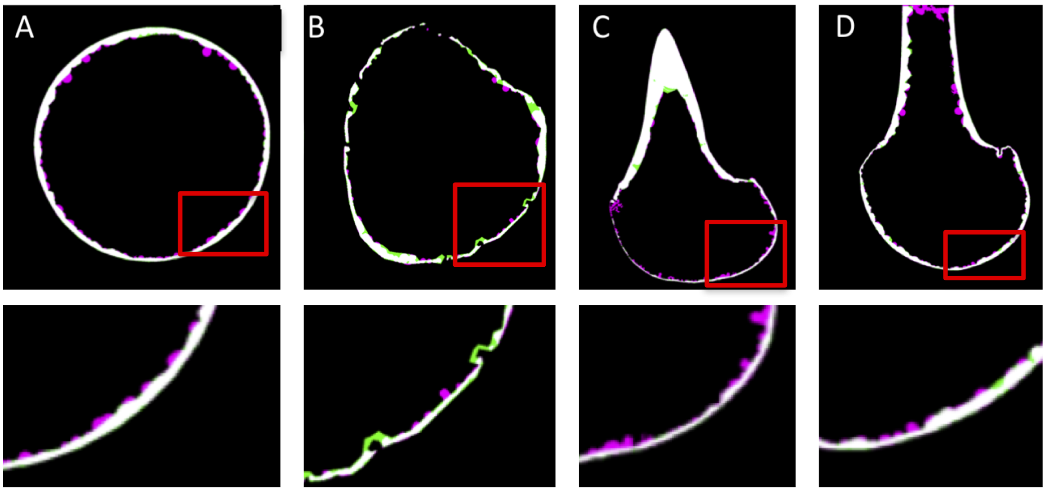

Figure 8.: Overlay of manual vs. algorithm segmentation for (A) femoral head, (B) femoral neck, (C) chimpanzee lateral condyle, and (D) gorilla lateral condyle. White displays the regions of overlapping segmentation, green displays manually segmented bone not present in the algorithm segmentation, and magenta displays algorithm segmented bone not present in the manual segmentation.

Previous attempts at identifying cortical boundaries were based on profiling the Hounsfield unit (HU) values along a line passing through the cortex. However, image noise and partial volume effects complicate the identification of a single HU threshold for segmentation, and either a mean HU value (Kang et al. 2003) or several threshold values must be used to create inner and outer borders (Buie et al. 2007; Lublinsky et al. 2007). Others have proposed using the normal vectors from an outer contour, again based on a threshold unit, in combination with morphological operations using kernel sizes derived from the trabecular structure to minimize artificial changes in structure (Lublinsky et al. 2007; Pahr and Zysset 2009; Gross et al. 2014).

Segmentation requires the capacity to distinguish the thicker region of cortical bone from trabecular bone, but may not be possible at joint surfaces where subchondral bone is thin. Morphological operations use a combination of processes such as opening/closing and erosion/dilation to mask and separate cortical and trabecular bone. The amount of bone to open/close or erode/dilate is determined by a kernel or structuring element size, which may be determined iteratively or via average trabecular thickness in the region of interest (Buie et al. 2007; Gross et al. 2014). This process may be problematic in complex trabecular bone and thin subchondral bone such that only a very large kernel size will work with subchondral bone, and thus will obscure small features and variations in the bony shell. Current methods may work well with bony areas that have less trabeculae or bones with less complex trabecular structure (i.e. in the bone shaft, or smaller bones like the metacarpal/tarsal). However, when the trabecular structure is highly complex and closely connected to the subchondral bone, such as at a joint (knee or hip), the results are sensitive to the thresholding and morphological opening/closing operations.

Here we propose that once a binarized image is obtained, the structure itself provides a reliable and unbiased means for separating the cortex from the remaining bone. The results presented were obtained using the same code for all datasets, but modifications can be made in the code to allow for greater segmentation accuracy. The user inputs that can be changed relate to the border search parameters and the size of the section of image to analyze at one time.

The accuracy of this algorithm is highly dependent on the thresholding process of the initial micro-CT images and other segmentation procedures. The true bone border can be affected by pixel-wide gaps in the bone border. Secondly, CT noise artifacts can mar sections of the bone border, especially where the border is concave, causing complications when identifying the bone border. Our evaluation of the initial border provides a means of ensuring that a continuous border exists, but the quality of the input binarized image remains a significant determinant of the resulting morphological measurements.

However, once binarized our algorithm for separating subchondral and trabecular bone allows for an effective analysis of isolated subchondral and trabecular properties across joint surfaces. This information is useful for a range of questions in comparative biology and clinical applications. For example, the spatial distribution of subchondral density and thickness across joint surfaces has been used to identify normal and pathological patterns of joint loading in human and other mammals (Müller-Gerbl et al. 1992; Carlson and Patel 2006; Pontzer et al. 2006; Su 2011; Madry et al. 2010). This is also clinically relevant since local (re)modeling responses in subchondral bone may be implicated in osteoarthritis.

The body of evidence suggesting that osteoarthritis is a disease that is initiated in subchondral bone is growing. Having the capacity to repeatably identify spatially specific changes in subchondral bone is critical to understanding how subchondral bone serves as an energy absorbing material to dissipate stresses during everyday loading of the joint (Madry et al. 2010; Müller-Gerbl et al. 1992)(Madry, van Dijk, & Mueller-Gerbl, 2010). Similarly, this method allows quantification of trabecular structures and properties across joint surfaces without interference or confounding effects of cortical/subchondral bone. The development of automated processing techniques - such as the one presented here - for high resolution data will allow for more thorough analyses over larger spatial regions and improve full-field characterizations of structure in complex materials.

Acknowledgements

We are grateful for the assistance of Kristian Carlson, Elizabeth Lee, America Guerra, Travis Ross, VMIL, Harvard Center for Nanoscale Systems, Iwona Dobrucka, Wawrzyniec Dobrucki, Leo Fabr, and the Beckman Molecular Imaging Lab for their assistance in data collection and processing.

Disclosure statement

The authors have no conflicts of interest to disclose.

Funding

Funding for this study was provided by National Science Foundation BCS-1638756, The Leakey Foundation, and the University of Illinois Research Board.

References

Buie HR, Campbell GM, Klinck RJ, MacNeil JA, Boyd SK. 2007. Automatic segmentation of cortical and trabecular compartments based on a dual threshold technique for in vivo micro-CT bone analysis. Bone. 41(4):505–15. Available from: http://www.ncbi.nlm.nih.gov/pubmed/17693147.

Carlson KJ, Jashashvili T, Houghton K, Westaway MC, Patel BA. 2013. Joint Loads in Marsupial Ankles Reflect Habitual Bipedalism versus Quadrupedalism. PLoS ONE. 8(3):e58811. Available from: http://dx.plos.org/10.1371/journal.pone.0058811.

Carlson KJ, Patel BA. 2006. Habitual use of the primate forelimb is reflected in the material properties of subchondral bone in the distal radius. Journal of Anatomy. 208(6):659–670.

Currey JD. 2002. Bones: Structure and Mechanics. Princeton: Princeton University Press.

Doube M, Klosowski MM, Arganda-Carreras I, Cordelières FP, Dougherty RP, Jackson JS, Schmid B, Hutchinson JR, Shefelbine SJ. 2010. BoneJ: free and extensible bone image analysis in ImageJ. Bone. 47(6):1076–1079.

Fajardo RJ, Müller R, Ketcham Ra, Colbert M. 2007. Nonhuman anthropoid primate femoral neck trabecular architecture and its relationship to locomotor mode. The Anatomical Record. 290(4):422–436. Available from: http://www.ncbi.nlm.nih.gov/pubmed/17514766.

Fox MC, Carlson KJ, Ryan T, Kersh ME, Polk JD. 2016. Reconstructing knee posture in humans, chimpanzees and gorillas: subchondral and trabecular signals. American Journal of Physical Anthropology. 159:146.

Gross T, Kivell TL, Skinner MM, Nguyen NH, Pahr DH. 2014. A CT-image-based framework for the holistic analysis of cortical and trabecular bone morphology. Palaeontologia Electronica. 17(3).

Hildebrand T, Rüegsegger P. 1997. A new method for the model-independent assessment of thickness in three-dimensional images. Journal of microscopy. 185(1):67–75.

Huiskes R, Ruimerman R, van Lenthe GH, Janssen JD. 2000. Effects of mechanical forces on maintenance and adaptation of form in trabecular bone. Nature. 405(June):704–706.

Kang Y, Engelke K, Kalender Wa. 2003. A new accurate and precise 3-D segmentation method for skeletal structures in volumetric CT data. IEEE transactions on medical imaging. 22(5):586–98. Available from: http://www.ncbi.nlm.nih.gov/pubmed/12846428.

Kivell TL. 2016. A review of trabecular bone functional adaptation: what have we learned from trabecular analyses in extant hominoids and what can we apply to fossils? Journal of Anatomy. 228(4):569–594. Available from: http://doi.wiley.com/10.1111/joa.12446.

Lublinsky S, Ozcivici E, Judex S. 2007. An Automated Algorithm to Detect the Trabecular-Cortical Bone Interface in Micro-Computed Tomographic Images. Calcified Tissue International. 81(4):285–293. Available from: http://download.springer.com/static/pdf/126/253A10.1007252Fs00223-007-9063-8.pdf.

Madry H, van Dijk CN, Mueller-Gerbl M. 2010. The basic science of the subchondral bone. Knee surgery, sports traumatology, arthroscopy. 18(4):419–433.

Müller-Gerbl M, Putz R, Kenn R. 1992. Demonstration of subchondral bone density patterns by three-dimensional ct osteoabsorptiometry as a noninvasive method for in vivo assessment of individual long-term stresses in joints. Journal of bone and mineral research. 7(S2).

Pahr DH, Zysset PK. 2009. From high-resolution CT data to finite element models: devleopment of an integrated modular framework. Computer Methods in Biomechanics and Biomedical Engineering. 12(1):45–57.

Pal NR, Pal SK. 1993. A review on image segmentation techniques. Pattern recognition. 26(9):1277–1294.

Polk JD, Blumenfeld J, Ahluwalia D. 2008a. Knee posture predicted from subchondral apparent density in the distal femur: an experimental validation. The anatomical record. 291(3):293–302.

Polk JD, Blumenfeld J, Ahluwalia K. 2008b. Knee Posture Predicted from Subchondral Apparent Density in the Distal Femur: An Experimental Validation. The Anatomical Record: Advances in Integrative Anatomy and Evolutionary Biology. 291(3):293–302. Available from: http://www.ncbi.nlm.nih.gov/pubmed/18286608 http://doi.wiley.com/10.1002/ar.20653.

Pontzer H, Lieberman DE, Momin E, Devlin MJ, Polk JD, Hallgrímsson B, Cooper DML. 2006. Trabecular bone in the bird knee responds with high sensitivity to changes in load orientation. The Journal of experimental biology. 209(Pt 1):57–65.

Pugh JW, Radin EL, Rose RM. 1974. Quantitative studies of human subchondral cancellous bone. The Journal of Bone and Joint Surgery (A). 56(2):313–321.

Radin EL, Paul IL, Lowy M. 1970. A comparison of the dynamic force transmitting properties of subchondral bone and articular cartilage. The Journal of bone and joint surgery American volume. 52(3):444–456.

Ryan TM, Ketcham RA. 2002. Femoral head trabecular bone structure in two omomyid primates. Journal of Human Evolution. 43(2):241–263. Available from: http://linkinghub.elsevier.com/retrieve/pii/S0047248402905750.

Ryan TM, Walker A. 2010. Trabecular bone structure in the humeral and femoral heads of anthropoid primates. The Anatomical Record. 293(4):719–729. Available from: http://www.ncbi.nlm.nih.gov/pubmed/20235327.

Su A. 2011. The functional morphology of subchondral and trabecular bone in the hominoid tibiotalar joint (Doctoral dissertation) [PhD Dissertation]. Available from ProQuest Dissertations and Theses database. (UMI No. 3474582). Available from: http://search.proquest.com.proxy2.library.illinois.edu/docview/897963480?accountid=14553.

Su A, Wallace IJ, Nakatsukasa M. 2013. Trabecular bone anisotropy and orientation in an Early Pleistocene hominin talus from East Turkana, Kenya. Journal of Human Evolution. 64(6):667–677. Available from: http://www.ncbi.nlm.nih.gov/pubmed/23601236 http://linkinghub.elsevier.com/retrieve/pii/S0047248413000754.

Wolff J. 1892. Das Gesetz der Transformation der Knochen (The Law of Bone Remodeling). Berlin: Verlag von August Hirschwald.